Water-stable boron-doped boron nitride photocatalyst for visible light-driven H_2 evolution and CO_2 photoreduction

Ravi B. Shankar[a], Daphné Lubert-Perquel[b,†], Elan Mistry[c], Irena Nevjestic,[b] Sandrine Heutz[b] and Camille Petit[a*]

[a]Barrer Centre, Department of Chemical Engineering, Imperial College London, South Kensington Campus, Exhibition Road, London SW7 2AZ, United Kingdom

[b]London Centre for Nanotechnology and Department of Materials, Imperial College London, South Kensington Campus, Prince's Consort Road, London SW7 2BP, United Kingdom

[c]Department of Chemistry, Imperial College London, South Kensington Campus, Exhibition Road, London SW7 2AZ, United Kingdom

[†]Current address: National High Magnetic Field Laboratory, Tallahassee, FL 32306 (U.S.A.)

*Corresponding author:

E-mail: camille.petit@imperial.ac.uk; Phone: +44 (0)20 7594 3182 (C. Petit)

Abstract

Developing robust, multifunctional photocatalysts that can facilitate both hydrogen evolution *via* photoreforming of water and gas phase CO_2 photoreduction is highly desirable with the long-term vision of integrated photocatalytic setups. Here, we present a new addition to the boron nitride (BN) photocatalyst material platform, boron-doped boron oxynitride (B-BNO), capable of fulfilling this goal. Detailed EPR studies revealed hyperfine interactions between free charges located on discrete OB_3 sites, exhibiting an out-of-plane symmetry, and the nuclei of neighbouring boron atoms. This material resolves two long-standing bottlenecks associated to BN-based materials concomitantly: instability in water and lack of photoactivity under visible light. We show that B-BNO maintains prolonged stability in water for at least three straight days and can facilitate both liquid phase H_2 evolution and gas phase CO_2 photoreduction, using UV-Vis and deep visible irradiation (λ > 550 nm), without any co-catalysts. The evolution rates, apparent quantum yields, and selectivities observed for both reactions with B-BNO exceed those of its porous BNO counterpart, P25 TiO_2 and bulk g-C_3N_4. This work provides scope to expand the BN photocatalyst platform to a wider range of reactions.

Keywords: boron nitride, photocatalysis, boron doping, solar fuels, H_2 evolution, CO_2 photoreduction

Introduction

With the ongoing efforts to stem the flow of anthropogenic CO_2 emissions, the share of renewables is projected to increase in the years and decades to come in the quest to transition from a fossil fuel dominant energy infrastructure to a sustainable energy portfolio.[1] The solar-driven production of fuels and valuable chemicals *via* photocatalysis represents one such energy generation route, allowing one to directly harness the abundance of incident sunlight. Common solar fuels obtained through this technology include H_2 derived from water splitting or photoreforming of water, and carbon-based molecules (e.g. CO, CH_4, CH_3OH, etc…) derived from CO_2 photoreduction.[2] Aside from solar fuel production, there have been recent efforts to utilize photocatalysis to synthesize other feedstock commodity chemicals, such as ammonia (NH_3) *via* photocatalytic nitrogen fixation[3, 4] and hydrogen peroxide (H_2O_2) *via* the solar-driven anthraquinone process[5].

In contrast to studies pertaining to H_2 evolution *via* photocatalytic water splitting, which have been rife since the pioneering works of Fujishima and Honda (1972)[6] and Inoue *et al.* (1979)[7], literature on catalysts for CO_2 photoreduction is comparatively less extensive. Indeed, the multiple electron transfer mechanism required for CO_2 photoreduction certainly presents increased thermodynamic barriers and kinetic limitations to overcome in comparison to water splitting, which only requires a two-electron transfer process. Designing robust photocatalysts from earth abundant elements, which can efficiently harness sunlight to drive this heterogeneous photocatalytic reaction, remains an on-going challenge in the field of solar fuels synthesis. To this end, researchers have investigated a plethora of materials, both porous and non-porous, as potentially viable photocatalysts. Examples of such materials include: derivatives of TiO_2[8-12], metal oxides[11, 13-15], oxynitrides[16-19], carbon nitrides[20-25], metal organic frameworks[8, 10, 26], covalent organic frameworks[27-29], linear conjugated polymers[30-33], and composites thereof[8, 10, 25, 34].

In a recent study, we focused on porous boron oxynitride (BNO)[35], a material that is gaining attention in the photocatalysis community.[21, 25, 35-42] Porous BNO exhibits key properties of an ideal photocatalyst, with the compelling features being its tuneable chemistry/photochemistry, which facilitate a tailored band structure *a priori*.[43] However, prior to this work[35], porous BNO had never been studied for CO_2 photoreduction. In our proof-of-concept study, we reported a porous BNO material that could function simultaneously as an adsorbent and semiconductor to facilitate combined gas phase CO_2 capture and photoreduction, using both UV and visible light, under ambient conditions without any co-catalyst. We showed that the rate performance of CO_2 photoreduction to CO with porous BNO was higher than that of the benchmark in the field, *i.e.* P25 TiO_2. Porous BNO maintained 85% of its performance over multiple catalytic cycles.

The results from this work have enabled us to introduce porous BNO as a new platform photocatalyst material. However, the material presented two key bottlenecks that limits its application and performance. The first bottleneck pertains to the instability of the porous BNO material in the presence of water.[44-47] In a recent study, we showed that porous BNO loses virtually all of its high surface area and porosity, and decomposes rapidly in the presence of water to form boron oxide and ammonia.[44] As such, this severely restricts the application of porous BNO to solely gas phase photocatalytic reactions and renders the employment for liquid phase reactions, such as H_2 evolution, unfeasible and impractical. The second bottleneck pertains to the limited photoactivity exhibited by porous BNO in the visible region of the light spectrum. Whilst porous BNO indeed facilitated CO_2 photoreduction to CO under pure visible light, the rate performance was much lower compared to UV-Vis irradiation. With 55% of the solar spectrum concentrated as visible light, it is essential to expand the BN photocatalyst functionality to deeper within the visible-light region, and thereby increase its rate performance. We therefore pose the key research question that frames this study: *can we synthesize a water stable BNO material that harvests light across the visible region of the spectrum?*

With this in mind, we expand the BN photocatalyst material platform by studying boron-doped boron oxynitride (B-BNO) for both H_2 generation and CO_2 photoreduction. This material exhibits semiconducting properties and photophysics not previously observed in BN materials, with hyperfine interactions between the unpaired electron, located on isolated OB_3 sites, and the nuclear spin of neighbouring boron atoms, as shown by room temperature EPR spectra. The free radical in these discrete OB_3 sites exhibits an out-of-plane symmetry, akin to a $2p_z$ antibonding orbital. As a progression from our proof-of-concept study[35], we show that B-BNO can overcome the two bottlenecks associated to the benchmark BN photocatalyst, porous BNO, namely instability in water and lack of light harvesting in the visible region. In doing so, B-BNO can facilitate H_2 evolution *via* the photoreforming of water in a simple solid/liquid phase set-up under ambient conditions, without the use of a co-catalyst. In addition, B-BNO can serve as a multifunctional photocatalyst and photoreduce CO_2 to CO in the gas phase under both UV-Vis and deep visible ($\lambda > 550$ nm) irradiation, with evolution rates higher than porous BNO, P25 TiO_2, and bulk graphitic carbon nitride (g-C_3N_4). This is first time that a BN-based material is able to function as a semiconductor to facilitate both liquid phase H_2 evolution and CO_2 photoreduction, under both UV-Vis and deep visible irradiation, without the use of additional element dopants (outside of the constituent B, N and O atoms) or co-catalysts. This work could pave the way for the expansion and further development of the BN photocatalyst platform.

Results and discussion

To gain insight into the morphology and structure of the B-BNO material in comparison to porous BNO, we first collected powder XRD patterns (Figures 1a). The XRD patterns in Figure 1a confirm the enhanced crystallinity of B-BNO in comparison to porous BNO through the sharper peaks at 2θ values of 26° and 44°, corresponding to the (002) and (100) planes, respectively.[49, 53, 54] This indicates longer-range 3D/graphitic order in B-BNO in contrast to porous BNO, which exhibits an amorphous/turbostratic nature with significantly broader peaks at the same 2θ values. The d-spacing calculated from the XRD peak (002) for B-BNO and porous BNO is 3.4 Å and 3.5 Å, respectively. The d-spacing in porous BNO is only relevant to the pseudo-crystalline regions of the material.

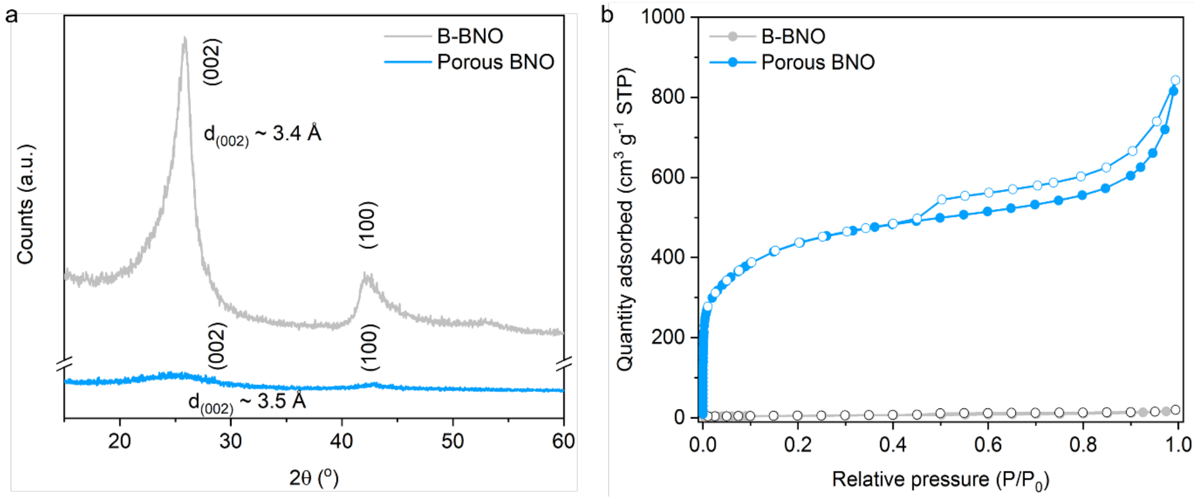

Figure 1 I Structure and morphology of the B-BNO sample compared to porous BNO. (**a**) Powder XRD patterns of B-BNO and porous BNO and (**b**) N_2 sorption isotherms for B-BNO and porous BNO measured at -196 °C.

To characterize the structural features of the material at the micro/nano-scale, we analyzed the specific surface area and porosity through nitrogen sorption at −196 °C (Figure 1b for isotherms, Supplementary Table 1 for textural parameters). The B-BNO sample displays a BET equivalent specific surface area of 18 m^2 g^{-1} and a total pore volume of 0.025 cm^3 g^{-1}, which are considerably lower than those for porous BNO (1585 m^2 g^{-1} and 1.10 cm^3 g^{-1}). This is to be expected given the prolonged high temperature synthesis required to synthesise B-BNO and the lack of precursors in the synthesis that are capable of releasing gases to form pores. The type I/IV isotherm with a type H3/H4 hysteresis loop observed for porous BNO indicates the presence of slit-shaped micro- and mesopores.

We analyzed the chemical composition and bonding types of B-BNO using FT-IR and XPS (Figure 2 and Supplementary Figures 2 and 3) and compared them to those of porous BNO. Both samples exhibit the two characteristic IR bands of BN at ~1380 cm^{-1} (in-plane B-N transverse stretching) and ~800 cm^{-1} (out-of-plane B-N-B bending).[55] We also observed a weak B-O band at ~1000 cm^{-1}, which is not observed in B-BNO (Figure 2a).[35, 43, 44] To gain further insight into the relative atomic surface composition and chemical states of the elements, we collected high resolution core level spectra through XPS. The fitted B 1*s* core level spectra for the starting amorphous boron precursor and the final B-BNO material are presented in Figure 2b. The complete fitted B 1*s*, N 1*s* and O 1*s* core level spectra for both B-BNO and porous BNO are presented in Supplementary Figures 2 and 3. The relative atomic compositions of both are presented in Supplementary Table 2. The key results from the XPS analysis are two-fold. Firstly, Figure 2c illustrates the complete nitrification of amorphous boron and incorporation of boron in the final B-BNO structure. Amorphous boron exhibits two peaks at binding energies of 187.6 eV, corresponding to B-B bonds in the icosahedral boron clusters, and 189.0 eV, corresponding to B-O bonds in oxides on the surface of the boron-rich clusters, where oxygen atoms are surrounded by several boron atoms (B_x-O).[56, 57] Further, a small peak at 193.2 eV is observed in amorphous boron, corresponding to a surface layer of boron oxide (B_2O_3).[56] Amorphous boron has a near-zero nitrogen content, which is a valuable aid in quantifying the extent of nitrification and conversion to BN. Both the B-B peak at 187.6 eV and the B_x-O peak at 189.0 eV are not observed in the B 1s spectrum of the final B-BNO material. Instead, we observe a distinct peak at 191.0 eV, corresponding to the B-N bond[49, 58, 59], and a smaller peak at 192.3 eV that we attribute to the boron oxynitride (B-O_x-N_{3-x}) species, which stems from the in-plane substitution of oxygen atoms in the BN lattice, as we have described in a prior study[35, 44]. The B-N and B-O_x-N_{3-x} peaks at 191.0 eV and 192.3 eV (Figure 2a), respectively, as well as an increase of 42 at. % in the relative nitrogen content (Figure 2c) confirms the formation of a BN material. The absence of the B-B peak at 188.2 eV, as well as the increase in relative atomic composition of boron (Figure 2c), in the B-BNO material indicate that boron has been successfully doped into BNO and the nature of doping is random atomic substitution as opposed to island formation of boron clusters.

The formation of BN is also confirmed through the fitted core level spectra N 1s which show the presence of B–N bonds (398.5 eV for N 1s, Supplementary Figure 4).[59] We also observe shake-up satellite peaks in the B 1*s* and N 1*s* core level spectra for B-BNO (Supplementary Figure 4), which provides evidence for the formation of an sp^2-hybridized hexagonal BN phase.[60, 61] We also note a small proportion of oxygen (3 at. %) in B-BNO with a peak at 192.3 eV and 533.1 eV for the B 1*s* and O 1*s* core level spectra, respectively, which we attribute to the aforementioned boron oxynitride ($B-O_x-N_{3-x}$) species. Whilst amorphous boron exhibited a relatively high carbon content (~ 13 at. %), the carbon content in the B-BNO sample was comparatively much lower (~1 at. %) and is linked to the presence of adventitious carbon impurities, *i.e.* not part of the material.

Next, we probed the optoelectronic properties of B-BNO through UV-vis diffuse reflectance spectroscopy. The absorption spectrum (Figure 2d) of the material clearly indicates a prominent red-shift when moving from porous BN to B-BNO, with an absorption edge shift from 320 nm to 730 nm. From the Tauc plot of the transformed Kubelka–Munk function against photon energy (Supplementary Figure 4), the B-BNO sample exhibits a deep visible band gap of 1.70 eV ± 0.05 eV, significantly lower than that of porous BNO (~3.55 eV ± 0.05 eV) (Supplementary Figure 4). We consider B-BNO and porous BNO as direct band-gap semiconductors based on literature.[62]

In our previous study[35], we were not able to infer whether the reduction in band gap from *h*-BN to porous BNO was related to the presence of functional groups, their specific location on the BN nanosheets or the introduction of porosity. However, the significant change in the semiconducting properties when transitioning from porous BNO to a non-porous B-BNO, suggests that this change can be attributed to the chemical modification, namely boron doping. We followed the same methodology as our previous study[35] to determine the band structure of B-BNO in comparison to porous BNO by measuring the valence band offset (ΔE_{VB}) and work function (Φ) through XPS measurements (Supplementary Figures 5 and 6). We note here that since the charge carriers are bound and trapped in a potential well, the energies relative to absolute vacuum are negative. Hence, the work function (Φ) and valence band offset (ΔE_{VB}) take negative values relative to absolute vacuum based on the notation outlined in our previous study.[35] B-BNO and porous BNO exhibited valence band offsets of -1.60 eV and -3.05 eV, respectively (Supplementary Figure 5). The work functions for B-BNO and porous BNO were determined to be -4.0 eV and -3.1 eV, respectively (Supplementary Figure 6).

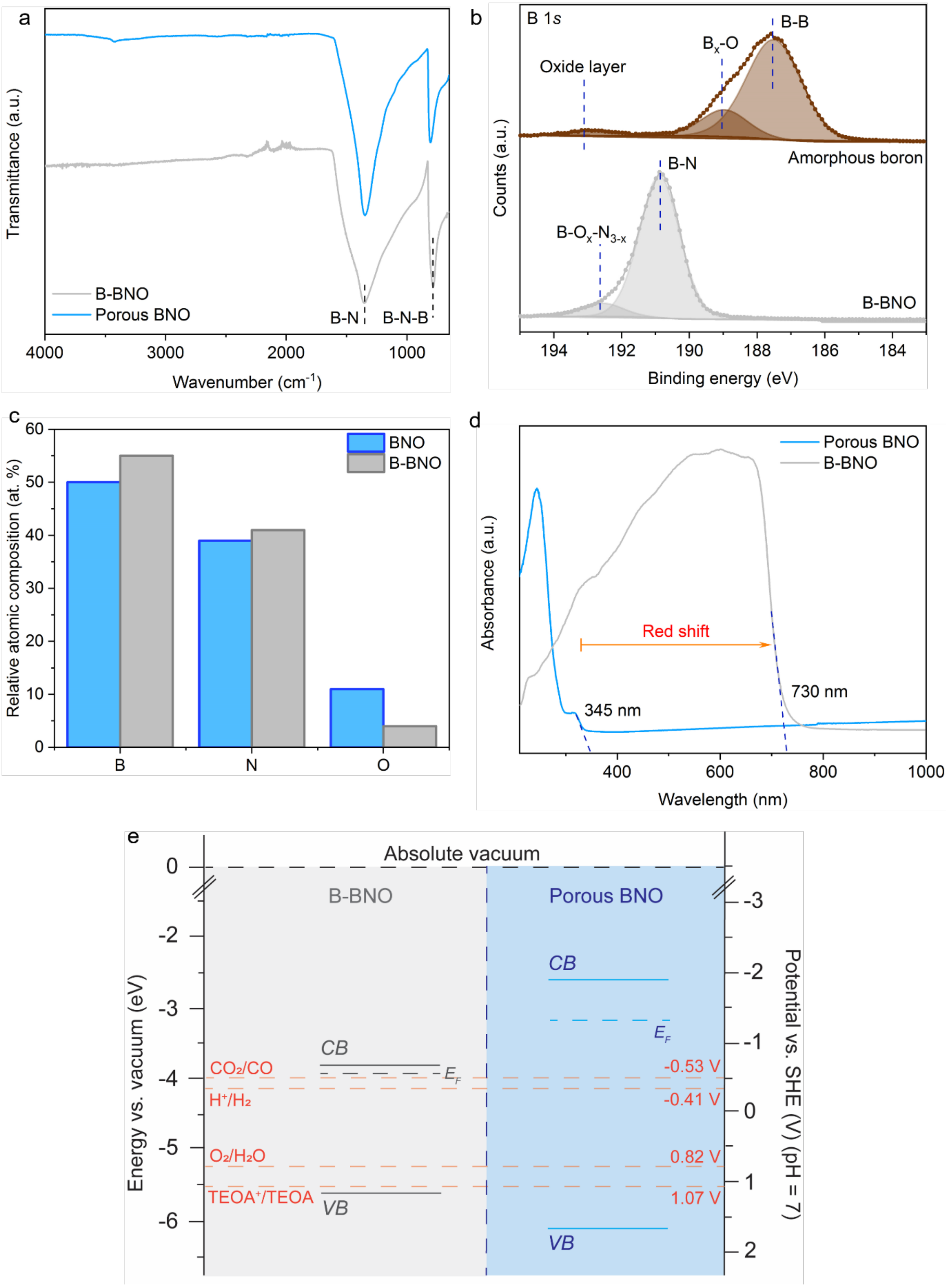

Figure 2 I Chemical, electronic and photophysical characterization of B-BNO and porous BNO. (**a**) FT-IR spectra of the as-synthesized B-BNO, with key characteristic bands highlighted, in comparison to porous BNO (**b**) Comparison of fitted B 1*s* core level spectra for

amorphous boron and B-BNO, (**c**) Relative atomic composition of B-BNO as obtained through XPS analysis, compared to porous BNO. (**d**) UV-Vis DRS absorption spectrum of the B-BNO sample compared to that of porous BNO, (**e**) Band structure for B-BNO and porous BNO on the absolute energy scale vs. vacuum with the conduction and valence bands, with the redox potentials for H^+/H_2, O_2/H_2O, $TEOA^+/TEOA$ and CO_2/CO illustrated.

By combining this data with the optical band gaps determined in Supplementary Figure 4, we determine the conduction and valence bands to be -3.90 eV and -5.60 eV for B-BNO and -2.60 eV and -6.15 eV for porous BNO. The complete band structures for B-BNO and porous BNO on the absolute energy scale vs. vacuum, with the redox potentials for H^+/H_2, $TEOA^+/TEOA$, O_2/H_2O and CO_2/CO vs. SHE at pH = 7 are presented in Figure 2e. The conduction and valence bands for both B-BNO and porous BNO straddle the redox potentials for both the photoreforming of water and CO_2 photoreduction systems, which is imperative for the material to be able to thermodynamically facilitate the reaction. We observe that the separation between the Fermi level and conduction band in B-BNO is smaller as compared to porous BNO (Figure 2e). This suggests that B-BNO exhibits a stronger n-type character than porous BNO, which is desirable for both H_2 evolution and CO_2 photoreduction. The band positions of B-BNO and porous BNO in Figure 2e indicate that the formation of a composite BNO photocatalyst *via* a type I heterojunction might be possible to enhance charge separation.

To investigate the paramagnetic species of the B-BNO compound, electron paramagnetic resonance (EPR) spectroscopy was used (Figure 3). The radical peak is attributed to the unpaired electron stemming from OB_3 sites, where an oxygen atom has substituted an interior nitrogen atom in the lattice and is surrounded by 3 neighbouring boron atoms.[35, 43] The B-BNO radical peak is significantly enhanced in the EPR spectra compared to the porous BNO (Figure 3a). Although the oxygen content in B-BNO is comparatively smaller to porous BNO (see Figure 2c), the increased boron content in B-BNO likely results in more OB_3 states. Further, the increased oxygen content in porous BNO increases the likelihood of forming conjugated O-B-O chains *via* adjacent OB_3 states, which is a diamagnetic state that does not contribute to the EPR signal.[35, 43] The *g*-values are also shifted between the two compounds, which is expected as *g*-values are highly sensitive to the chemical environment of radicals. Moreover, fine structure features are apparent in the B-BNO spectrum, which can be attributed to hyperfine interactions. Hyperfine interactions refer to interactions between an unpaired electron and the nuclei of the surrounding neighbour atoms. Isotropic hyperfine interactions have previously been reported in BN based materials, where the unpaired electron stabilised in a nitrogen vacancy interacts with 3 boron nuclei.[63, 64] The peak splitting observed in the B-BNO spectrum originates from 10 lines. Considering ^{11}B, the most abundant isotope of boron with I = 3/2, 3 boron nuclei must be interacting according to the 2NI + 1 rule. A simulation with least square fitting was used to determine the hyperfine tensor (Figure 3b). The hyperfine tensor was found to have rhombic anisotropy, with an isotropic component A_{iso} = 12 MHz (0.43 mT) and an anisotropic dipolar component [10 -2 -8] MHz. Previous work has shown that B-BNO is a planar system with the OB_3 radical in a $2p_z$ antibonding orbital.[65] Our EPR results confirm that this is also what is observed here, as the hyperfine tensor is in line with what can be predicted for a H bound to a p-radical, such as CH_3.[66]

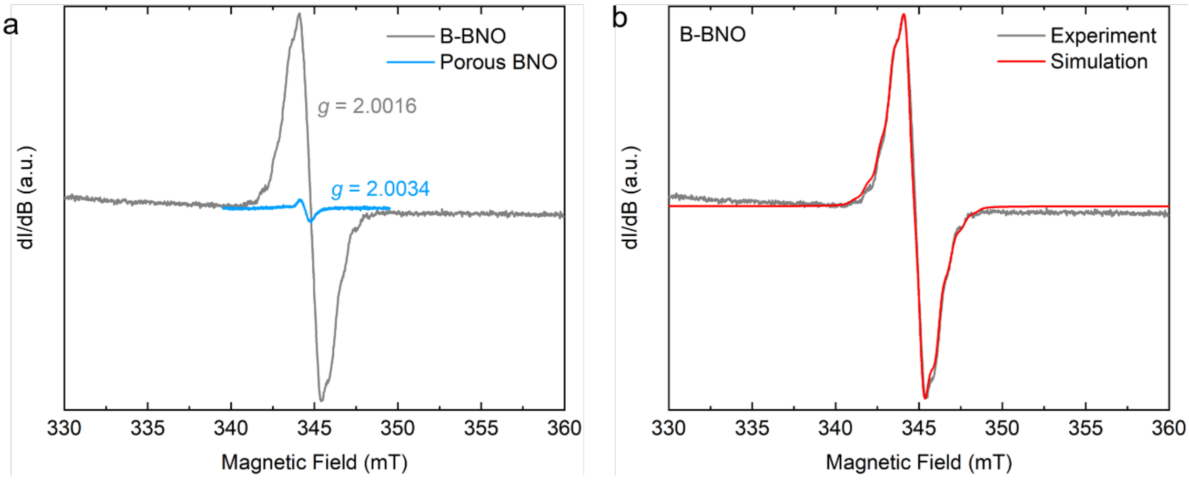

Figure 3 I Paramagnetic characterisation of B-BNO compared to porous BNO. (**a**) Room temperature EPR spectra for B-BNO compared to the porous BNO used as reference with the *g*-values indicated. (**b**) Simulation of the EPR spectra for B-BNO showing hyperfine interactions.

The analyses above indicate that B-BNO can harvest light in the visible region of the spectrum, which was the first bottleneck of porous BNO. We now turn our attention to the second bottleneck of porous BNO, related to the instability in water. The B-BNO and porous BNO materials displayed contrasting responses to the stability test. The powder XRD patterns of the pristine and exposed B-BNO and porous BNO samples are presented in Figures 4a and 4b. No evident change in the XRD patterns nor the formation of additional peaks were observed after 3 hours, while the formation of small peaks at 34° and 36° are observed after 72 hours (Figure 4a), possibly attributed to facets of amorphous boron.[56] In contrast, we observe a significant increase the relative intensity of the (002) and (101) peaks after 3 hours of water exposure for porous BNO. This feature is linked to the decomposition of the amorphous portion of BNO while the crystalline portion remains (Figure 4b), as observed in other studies.[44, 45, 47] The formation of additional peaks at 31° and 33° are observed in porous BNO, possibly linked to facets in boron oxide.[67] Further, virtually the entire specific surface area and porosity was lost in porous BNO after minimal exposure to water, whereas B-BNO maintained the original, albeit low, surface area and porosity (Supplementary Figure 7).

We then conducted XPS on the B-BNO and porous BNO samples exposed to water in the stability test to investigate potential chemical changes, namely the formation of boron oxide. The relative atomic compositions of pristine and exposed B-BNO and porous BNO are presented in Figures 4c and 4d, respectively. The B 1*s*, N 1*s* and O 1*s* core level spectra for the samples after the stability test are presented in Supplementary Figures 8 and 9. The relative atomic compositions of the pristine and water-exposed samples are presented in Supplementary Table 2. B-BNO maintained the same relative atomic chemical composition as the pristine sample, both after 3 hours and 72 hours of immersion in water (Figure 4c), and no formation of an oxide shoulder peak was observed in the B 1*s* spectrum (Supplementary Figure 8). Unlike B-BNO, the porous BNO sample exhibited a prominent shoulder peak in the B 1*s* spectrum at 193.1 eV after exposure to water, related to boron oxide (Supplementary Figure 9).[44, 68-70] This result is in agreement with the reaction observed and described in the literature, where boron nitride reacts with water to form boron oxide and ammonia.[44, 46] Further evidence of the decomposition is shown in Figure 4d, not only by the increase in the oxygen content, but also by the relative percentage of nitrogen decreasing, which is in line with the formation of ammonia.

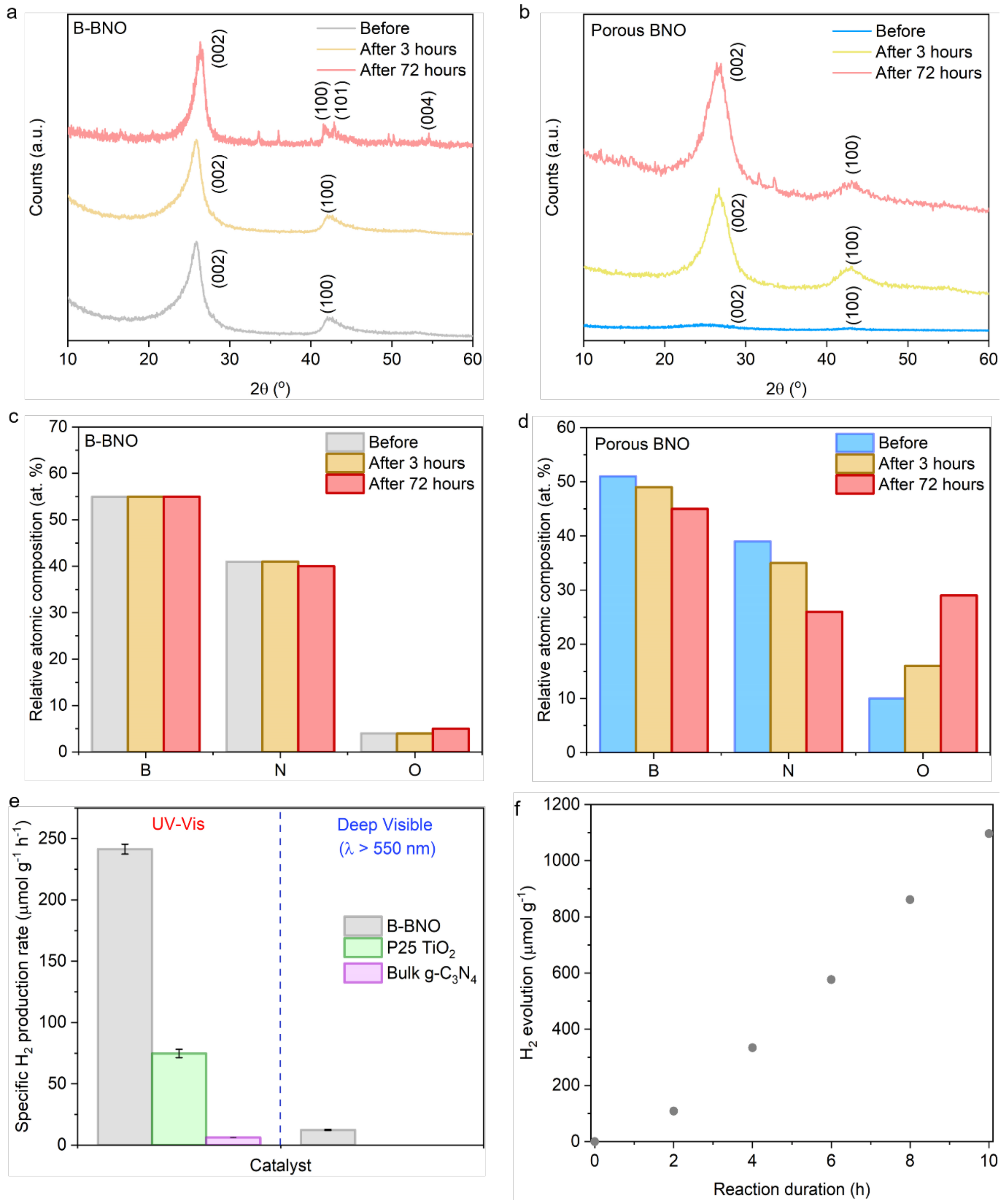

Figure 4 I Comparison of water stability of B-BNO and porous BNO and photocatalytic testing of B-BNO for H_2 evolution through photoreforming of water. (**a**) Powder XRD patterns of B-BNO before and after exposure to DI water at 25 °C for 3 hours and 72 hours,

(**b**) Powder XRD patterns of porous BNO before and after exposure to DI water at 25 °C for 3 hours and 72 hours, (**c**) Relative atomic composition of B-BNO before and after exposure to DI water at 25 °C for 3 hours and 72 hours, obtained through XPS, (**d**) Relative atomic composition of porous BNO before and after exposure to DI water at 25 °C for 3 hours and 72 hours, obtained through XPS, (**e**) Specific production rate of H_2 for B-BNO compared to P25 TiO_2, and bulk carbon nitride (g-C_3N_4) as reference materials, under UV-Vis and pure deep visible light irradiation ($\lambda > 550$ nm) and 0.1 м TEOA (aq) sacrificial donor solution (300 W Xe arc lamp, 12.5 cm distance from catalyst to lamp source, 3 hours, 25 °C). Average intensity at the catalyst surface was 1730 ± 26 W m^{-2} without the UV-filter and 1530 ± 12 W m^{-2} with the deep visible filter ($\lambda > 550$ nm), (**f**) Kinetic study illustrating photocatalytic H_2 evolution from B-BNO as a function of time under UV-Vis irradiation (same lamp, intensity and reactor settings as before).

Overall, the results indicate that B-BNO is a water stable BN based material for at least three straight days, which successfully addresses the second bottleneck of the porous BNO catalyst. Moreover, the results from Figures 2-4 together show that we have synthesised a water-stable, photoactive BN material that is capable of functioning as a semiconductor – the underlying aim of this study.

Next, we tested B-BNO as a photocatalyst to facilitate hydrogen evolution *via* the photoreforming of water under UV-Vis and pure deep visible ($\lambda > 550$ nm) irradiation, in a 0.1 м TEOA (aq) solution, without the presence of a co-catalyst. The performance was compared to 'reference' materials, *i.e.* P25 TiO_2 and bulk graphitic carbon nitride (g-C_3N_4). P25 TiO_2 is a benchmark commercial material in the field, which enables comparison with other groups' work, despite differences in experimental set-ups. Being a commercial material, P25 acts as an internal reference and its use for comparison is in part of the guidance in the field.[71] Graphitic carbon nitride is the closest material in terms of chemistry and structure to boron nitride and a well-known visible light photocatalyst for H_2 evolution and CO_2 photoreduction.[39, 72] Since porous BNO is unstable in water, we did not test for photoreforming of water.

Under the conditions, B-BNO drove the photoreforming of water with an average specific H_2 production rate of 241.45 μmol g^{-1} h^{-1} under UV-Vis irradiation and 12.35 μmol g^{-1} h^{-1} under pure deep visible irradiation ($\lambda > 550$ nm). P25 TiO_2 and bulk g-C_3N_4 yielded an average specific H_2 production rate of 74.75 μmol g^{-1} h^{-1} and 6.25 μmol g^{-1} h^{-1} under UV-Vis irradiation, which shows that B-BNO has a substantially higher photocatalytic output over the full UV-Vis spectrum than the reference materials. The apparent quantum yield (AQY) for B-BNO was determined to be 0.23% across the full UV-Vis spectrum of the Xe arc lamp source (270 – 900 nm) and 0.02% in the deep visible region of the spectrum (550 – 900 nm) (see Supplementary Information for calculation procedure and error analysis). Huang *et al.* reported a similar AQY (0.54% at $\lambda = 405$ nm) associated to H_2 evolution with carbon-doped BN and a platinum co-catalyst.[40] No discussion regarding the water stability of the material was presented. The AQY of B-BNO for H_2 evolution was more than double that of P25 TiO_2 (0.07%) and an order of magnitude higher than bulk g-C_3N_4 (0.01%). The specific H_2 evolution rates and apparent quantum yields of all the materials investigated in this study are tabulated in Supplementary Table 3. None of the reference materials exhibited any photoactivity under deep visible irradiation ($\lambda > 550$ nm), which is to be expected given their higher band gaps (3.55 eV, 3.20 eV and 2.72 eV for porous BNO, P25 TiO_2, and bulk g-C_3N_4 respectively). Hence, B-BNO offers both a wider and greater light harvesting efficiency than porous BNO and reference materials for H_2 evolution *via* photoreforming of water.

We confirmed the origin of H_2 through a number of control tests: absence of catalyst and dark mode (Supplementary Table 4). In the absence of a catalyst and under dark mode, no H_2 was detected. To assess the source of protons, we used D_2O as the solvent, whilst maintaining the same catalyst preparation method and reaction conditions from the original system. When D_2O was used instead of H_2O, only D_2 was detected under mass spectrometry (Supplementary Figure 10). The results indicate that water serves as the proton source and TEOA acts as the electron donor. B-BNO maintained its photoactivity over a 10-hour testing period (see kinetic study, Figure 4f). The combined results across

Figures 2-4 show that we have produced a new addition to the BN photocatalyst platform that exhibits: (i) prolonged water stability, (ii) unique semiconducting and photophysical properties, (iii) photoactivity in the visible region to facilitate H_2 evolution, and (iv) a constant H_2 evolution rate over 10 hours under UV-Vis irradiation.

Having achieved the underlying aims of this study, we subsequently investigated whether B-BNO could function as a multifunctional photocatalyst and facilitate combined CO_2 capture and photoreduction in the gas phase. The results from our previous study[35] would lead us to believe that a high surface area and porosity, as observed in porous BNO, would be required to facilitate this process. However, although B-BNO lacks surface area and porosity compared to its porous counterpart, testing the material for combined CO_2 capture and photoreduction in the gas phase can provide some insight into the role of porosity in BN photocatalysts and indicate whether the enhanced light harvesting capability can compensate for a potential loss in CO_2 adsorption. Moreover, several photocatalysts being tested in the literature for CO_2 photoreduction are non-porous yet show photocatalytic output. Prior to photocatalytic testing, we measured the CO_2 adsorption capacity of the material at the reaction conditions (25 ^{o}C, 0-1 bara) and compared to porous BNO and the 'reference' materials, *i.e.* P25 TiO_2 and carbon nitride. Unsurprisingly, porous BNO adsorbs significantly more CO_2 than B-BNO and the reference materials (Figure 5a, Supplementary Table 5), due to its higher porosity (Supplementary Table 1). Next, we tested B-BNO, porous BNO and the reference materials for the gas phase photoreduction of CO_2 under UV-vis and pure deep visible irradiation (λ > 550 nm), without doping or the presence of a co-catalyst. For all materials, after an irradiation time of 3 hours, CO was observed as the major product, with comparatively smaller quantities of CH_4 detected. Under these conditions, B-BNO drove the photoreduction of CO_2 with an average specific CO production rate of 6.53 μmol g^{-1} h^{-1} and an AQY of 0.019% across the UV-Vis spectrum (270 – 900 nm), which was almost order of magnitude higher than that of porous BNO (CO production rate of 0.61 μmol g^{-1} h^{-1} and AQY of 0.0019%). B-BNO also exhibited a higher specific CO production rate and AQY than those for the reference materials (1.01 μmol g^{-1} h^{-1} for P25 TiO_2 and 0.30 μmol g^{-1} h^{-1} for bulk g-C_3N_4). The same trend amongst the materials is also observed with regard to the minor product, CH_4 (Figure 5b and Supplementary Table 5). Further, B-BNO also exhibited the highest selectivity towards CO production (94.2 %) amongst the materials tested in this study (Supplementary Table 6). The specific CO and CH_4 evolution rates, AQYs and selectivities of all the materials investigated in this study are tabulated in Supplementary Tables 5 and 6, respectively. We note that porous BNO indeed displayed a higher specific CO production rate compared to P25 TiO_2 in our previous study.[35] A possible cause for this variation in trend could be the change in intensity and spread of the incident light irradiation on the material between the two studies. Overall, the results suggest that the extended light absorption to the deep visible range in B-BNO compensates the lower porosity and surface area. The difference in photophysics observed in Figure 3 between B-BNO and porous BNO may have influence as well.

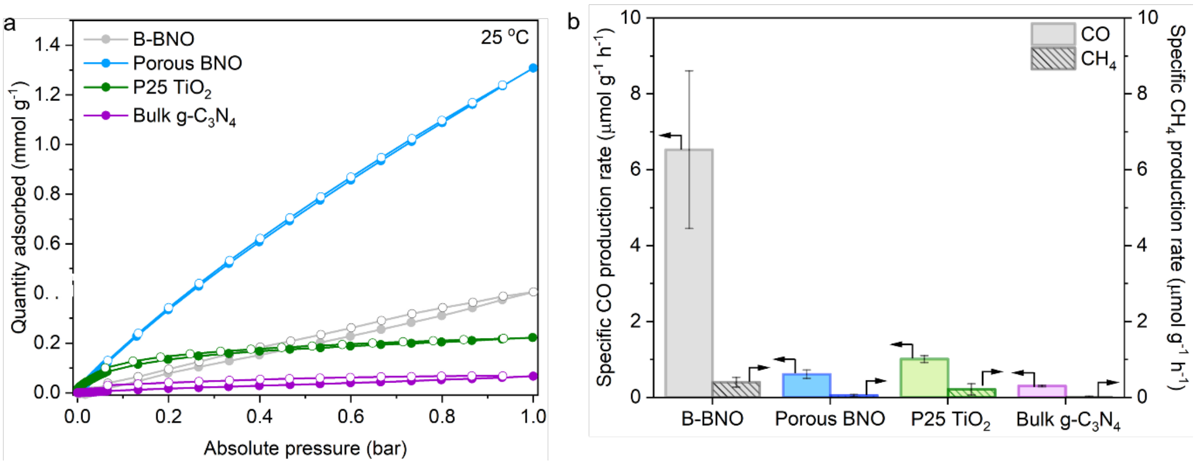

Figure 5 I Photocatalytic testing of B-BNO for gas phase CO_2 photoreduction. (**a**) CO_2 adsorption isotherms collected at 25 °C for the materials investigated in this study, (**b**) Specific production rates of CO and CH_4 for B-BNO, compared to porous BNO, P25 TiO_2, bulk carbon nitride (g-C_3N_4), as reference materials, under UV-vis irradiation and H_2 as a sacrificial agent (300 W Xe arc lamp, 9.5 cm distance from catalyst to lamp source, 3 hours, 25 °C). Intensity at the catalyst surface was 1850 ± 17 W m^{-2}.

We confirmed the origin of CO through a number of control tests: absence of catalyst, dark mode, and N_2/H_2 atmosphere (Supplementary Table 6). All supported the fact that the source of the CO evolved stems from the photocatalytic reduction of CO_2. To further substantiate this claim, we carried out isotopic experiments using $^{13}CO_2$. Aside from $^{13}CO_2$ being used as the feed gas in tandem with H_2 as the sacrificial agent, we maintained the same catalyst preparation method and reaction conditions from the original system. The gas chromatograms corresponding to the ^{13}CO peak (m/z = 29) and ^{12}CO (m/z = 28) under both dark and light conditions, as well as the mass spectra for the photocatalytic $^{13}CO_2$ reduction system are presented in Supplementary Figure 11. Here, 'dark' and 'light' refer to the pre- and post-reaction conditions. Under dark conditions, no ^{12}CO nor ^{13}CO is observed in the system. Under light conditions after the completion of the reaction, only ^{13}CO (m/z = 29) is observed in the gas chromatogram, with no peak for ^{12}CO (m/z = 28) observed. In accordance with this is the corresponding mass spectra that shows m/z = 45 ($^{13}CO_2$) and m/z = 29 (^{13}CO) are the dominant peaks. The results point to the formation of ^{13}CO and provides direct evidence that the origin of the evolved CO is indeed from the reduction of CO_2 itself.

Finally, we checked the stability of the B-BNO material through the XRD pattern of the used catalyst and did not observe any increase or change in crystallinity in comparison with the pristine sample after CO_2 photoreduction (Supplementary Figure 12). However, with porous BNO we observed a slight increase in crystallinity in the XRD pattern. This finding suggests that amorphous domains of the material degraded upon reaction. This is supported by N_2 sorption tests, which showed a 10% decrease in porosity after the CO_2 photoreduction. Notably though, the porous BN sample still maintained a high surface area and porosity of 1196 $m^2\ g^{-1}$ and 1.01 $cm^3\ g^{-1}$ (Supplementary Table 1). The B-BNO sample maintained the same surface area and porosity as the pristine sample, which is to be expected given that this level of stability was observed when exposed to liquid water, where decomposition is even more likely with BN materials (Supplementary Table 1). We did not observe any distinct changes in the FT-IR spectrum of the B-BNO nor the porous BNO sample after undergoing a CO_2 photoreduction cycle (Supplementary Figure 13).

Conclusions

In summary, we present a new addition to the BN photocatalyst material platform, boron-doped boron oxynitride (B-BNO). This material exhibits unique semiconducting properties and photophysics, with hyperfine interactions between the unpaired electrons and nuclear spin of boron, as shown by room temperature EPR spectra, providing information about the symmetry of the free radical. As a progression from our proof-of-concept study, we have shown that B-BNO can address and overcome the two bottlenecks associated to the benchmark BN photocatalyst, porous BNO, namely instability in water and lack of light harvesting in the visible region. In doing so, B-BNO can facilitate H_2 evolution *via* the photoreforming of water under in a simple solid/liquid phase set-up under ambient conditions, without the use of co-catalysts.

Unlike its porous counterpart, B-BNO is able to maintain structural and chemical stability in water for at least 72 hours and can evolve H_2 under both UV-Vis and deep visible ($\lambda > 550$ nm) irradiation, with average evolution rate of 241.5 μmol g^{-1} h^{-1} and 12.4 μmol g^{-1} h^{-1} and a corresponding AQY of 0.23% and 0.02%, respectively. This photocatalytic output and quantum yield are at least two orders of magnitude higher than porous BNO and bulk g-C_3N_4, and three times higher than benchmark in the field, *i.e.* P25 TiO_2. B-BNO exhibits a steady H_2 evolution rate over a single cycle. In addition, B-BNO can serve as a multifunctional photocatalyst and photoreduce CO_2 to CO and CH_4, with a 92.4% CO selectivity and AQY of 0.02%, in the gas phase. Again the evolution rates, CO selectivities and quantum yields significantly exceed those of porous BNO, P25 TiO_2 and bulk g-C_3N_4.

This is first time that a BN-based material is able to function as a semiconductor to facilitate both liquid phase H_2 evolution and gas phase CO_2 photoreduction, using both UV-Vis and deep visible irradiation, without the use of ‘foreign’ element dopants (outside of the constituent B, N and O atoms) or co-catalysts. Given the multifunctional photocatalytic performance of this material, there is considerable scope to scale-up the material synthesis and investigate potential device engineering. This would constitute a major stride in the field of solar fuels synthesis.

Experimental section

We synthesized boron-doped BNO (B-BNO) through a two-step procedure, based on the previous work of Weng *et al.* [43] and Rusanova and Gorchakova[48], as outlined below. The first step relies on the bottom-up synthesis of oxygen-doped boron nitride (BNO) using a mixture of boric acid and hexamethylenetetramine under an ammonia atmosphere at 1000 °C, as outlined by Weng *et al.*[43]. The second step, outlined by Rusanova and Gorchakova[48], involves the nitrification of amorphous boron in the presence of the as-synthesized BNO under an inert nitrogen atmosphere at elevated temperatures (>1300 °C) for prolonged time periods.

Synthesis of boron-doped boron oxynitride (B-BNO). The first step involves the bottom-up synthesis of oxygen-doped boron nitride (BNO) based on the procedure of Weng *et al.*[43] In a typical synthesis, boric acid (20 mmol, 1.237 g) (H_3BO_3, ACS reagent, 99.0 %, Sigma-Aldrich) and hexamethylenetetramine (HMTA) (40 mmol, 5.607 g) ($C_6H_{12}O_6$, molecular biology grade, Sigma-Aldrich) were added to deionized water (100 mL) at 90 °C under rapid stirring to form a boric acid-HMTA complex in solution. The solution was allowed to evaporate overnight until the resulting white powder was collected and subsequently dried for 24 hours at 90 °C in a drying oven. The dried material (approx. 1.4 g) was transferred to an alumina boat crucible, which was placed in a horizontal tubular furnace. The sample was initially degassed at ambient temperature for 30 minutes under pure ammonia flow, with the flowrate set to flow rate of 250 cm^3 min^{-1}. Once the degas was complete, the ammonia flow rate was decreased to 150 cm^3 min^{-1}, and the sample was heated from ambient temperature to 1000 °C with a ramp rate of 10 °C min^{-1}. This steady-state temperature was maintained for 3 hours, after which the samples were allowed to naturally cool to approximately 600 °C under the same ammonia flow rate. At this point, the ammonia flow was shut off and inert argon gas was flowed through at a rate of 100 cm^3 min^{-1} overnight until the furnace had cooled to room temperature. Upon completion of the synthesis, a yellow powder was obtained, which we refer to as BNO.

The second step of the synthesis involves the nitrification of amorphous boron in the presence of the as-synthesized BNO sample, according to Rusanova and Gorchakova.[48] The as-synthesized BNO sample and amorphous boron powder (>95%, Sigma Aldrich) in a ratio of 75 wt.% : 25 wt.% were mechanically mixed in an agate mortar to form a homogeneous powder, and then transferred to an alumina crucible, which was placed in a horizontal tubular furnace. The furnace was purged under nitrogen flow with a flow rate of 100 cm^3 min^{-1} overnight after which the sample was heated from ambient temperature to 1500 °C with a ramp rate of 10 °C min^{-1} under the same nitrogen flow rate. This steady-state temperature was maintained for 10 hours, after which the sample was allowed to naturally cool to room temperature, whilst maintaining the same flowrate of nitrogen. Upon completion of the synthesis, a light grey powder product was obtained, which we refer to as B-BNO. We chose a synthesis temperature of 1500 °C based on the results of Rusanova and Gorchakova[48], who showed that full nitrification of amorphous boron was achieved for a synthesis temperature of 1500 °C. We selected a reaction time of 10 hours for the same reason.

Synthesis of porous BNO. Porous BNO synthesis was based on the method developed by Marchesini *et al.*[49] In a typical synthesis, boric acid (10 mmol, 0.6177 g) (H_3BO_3, ACS reagent, 99.0 %, Sigma-Aldrich), urea (50 mmol, 3.000 g) (CH_4N_2O, molecular biology grade, Sigma-Aldrich), and melamine (10 mmol, 1.261 g) ($C_3H_6N_6$, ACS reagent, 99.0 %, Sigma-Aldrich), with a 1:1 molar ratio of boric acid to melamine and 1:5 molar ratio of boric acid to urea, were mechanically mixed together and finely ground for 5 minutes in an agate mortar to form a homogeneous powder. The finely ground powder was subsequently transferred to an alumina boat crucible, which was placed in a horizontal tubular furnace. The sample was initially degassed at ambient temperature for 3 hours under an inert nitrogen atmosphere (flow rate of 250 cm^3 min^{-1}). Once the degas was complete, the nitrogen flow rate was decreased to 50 cm^3 min^{-1}, and the sample was heated from ambient temperature to 1050 °C with a ramp rate of 10 °C min^{-1}. This steady-state temperature was maintained for 3.5 hours, after which the samples were allowed to naturally cool to room temperature, whilst maintaining the same nitrogen flow rate. Upon completion of the synthesis, a porous white powder was obtained, which we refer to as porous BNO.

Synthesis of bulk g-C_3N_4. In a typical synthesis, melamine (12 g) ($C_3H_6N_6$, ACS reagent, 99.0 %, Sigma-Aldrich) were weighed and transferred to an alumina crucible, which was placed in a muffle furnace. The sample was heated from ambient temperature to 560 °C with a ramp rate of 5 °C min^{-1}. This steady-state temperature was maintained for 4 hours, after which the sample was allowed to naturally cool to room temperature. Upon completion of the synthesis, a yellow solid product was obtained, which was subsequently ground in an agate mortar to form a fine, homogeneous powder, which we refer to as bulk g-C_3N_4.

P25 TiO_2 and amorphous boron. P25 TiO_2 and amorphous boron were industrially synthesised and obtained as follows: P25 TiO_2 (Sigma Aldrich, >99.5%, 21 nm primary particle size) and amorphous boron (≥95%, Sigma-Aldrich).

Characterization

Fourier transform infrared spectroscopy (FT-IR). The samples were first ground to a powder using an agate mortar. Subsequently, the spectra were obtained in the range of 500 – 4000 cm^{-1} using a Perkin-Elmer Spectrum 100 FT-IR spectrometer equipped with an attenuated total reflectance (ATR) accessory.

X-ray photoelectron spectroscopy (XPS) was employed to determine the relative elemental composition of the samples, the chemical states of the elements, the valence band off-set and secondary electron cut-off was conducted using a Thermo Scientific K-Alpha$^+$ X-ray Photoelectron Spectrometer equipped with a MXR3 Al Kα monochromated X-ray source (hv = 1486.6 eV). The samples were initially ground and mounted onto an XPS sample holder using a small rectangular piece of conductive carbon tape. The X-ray gun power was set to 72 W (6 mA and 12 kV). Survey scans were acquired using 200 eV pass energy, 0.5 eV step size and 100 ms (50 ms x 2 scans) dwell times. All of the high resolution core level spectra (B 1*s*, N 1*s*, C 1*s*, and O 1*s*) were obtained using a 20 eV pass energy and 0.1 eV step size. The valence band spectra were obtained using a 15 eV pass energy and 0.05 eV step size. The results were analysed using the Thermo Avantage data analysis program. Any charging effect in the core level and valence band measurements was mitigated by using a dual-beam flood gun that uses the combination of low energy electrons and argon ions.

Powder X-ray diffraction (XRD) was performed using a PANalytical X'Pert Pro X-ray diffractometer in reflection-transmission mode with a spinning stage (2 revolutions/second). An anode voltage of 40 kV and emission current of 20 mA were chosen as the operating conditions using a monochromatic Cu-Kα radiation source (λ = 1.54178 Å). The X'Celerator silicon strip detector was used in the diffractometer. The interplanar $d_{(002)}$-spacing was calculated from the powder XRD patterns using Bragg's law.

Nitrogen and CO_2 sorption isotherms were measured using a volumetric sorption analyser (Micrometrics 3 Flex) at -196 °C and 25 °C, respectively. The samples were initially degassed overnight at 140 °C at approximately 0.2 mbar pressure. Prior to the sorption isotherm measurement, the samples were further degassed in-situ for 4 hours at 120 °C. The equivalent specific surface areas of the samples were determined using the Brunauer-Emmett-Teller (BET) method.[50] The total pore volume was ascertained from the volume of

N_2 adsorbed at a relative pressure (P/P_0) of 0.97. The micropore volume was determined using the Dubnin-Radushkevich model.[51]

Water stability tests in water. We conducted a stability test by immersing a known mass (40 mg) of B-BNO and porous BNO, with two vials for each material of equal volumes (10 mL) of DI water at 25 °C. The two vials were used for different durations of water exposure in the stability test: 3 hours and 72 hours. The water was subsequently evaporated off and the samples were completely dried overnight at 120 °C in a drying oven prior to subsequent characterization.

Photocatalytic H_2 evolution. A liquid/solid Teflon-lined reactor setup was assembled to conduct the photocatalytic H_2 evolution tests. The photocatalyst (10 mg) was dispersed in 25 mL of 0.1 м (aq) triethanolamine (TEOA) solution inside a Teflon vessel with a magnetic stirrer bar. The vessel was inserted into a stainless steel closed reactor. Zero grade (99.998% purity) N_2 was fed at controlled rates using a mass flow controller (Omega Engineering, 0-100 mL min^{-1}). After the reactor was sealed, the system was purged with N_2 for 30 mins. The photoreactor was then vacuumed and replenished with N_2 ten times, after which the reactor was pressurised up to 1.40 bara, sealed and irradiated for 3 hours. A Xe arc lamp (300 W, $\lambda > 325$ nm, LOT Quantum Design), equipped with a water filter was used as the irradiation source with the distance from the lamp to the sample being 12.5 cm. A long pass visible filter ($\lambda < 550$ nm) (Thor Labs) was used to conduct the tests under deep visible light irradiation and the lamp emission spectra, both with and without the UV filters, are provided in Supplementary Figure 1. The intensity at the catalyst surface was measured to be 1730 ± 26 W m^{-2} without the visible filter and 1530 ± 12 W m^{-2} with the filter. The lamp intensity was acquired using a UV-Vis spectrophotometer with 280 – 900 nm range (StellarNet) and an average lamp intensity with standard deviation was calculated after three repeat measurements. The evolved gases were detected by a gas chromatograph (GC, Agilent Technologies) with HayeSep and molecular sieve columns in series, and thermal conductivity (TCD) and flame ionisation (FID) detectors. In addition, isotopic tracing experiments were performed with D_2O (Sigma Aldrich, >99.9%). The photocatalytic H_2 evolution tests were repeated three times for each material under the same reaction conditions to obtain an average specific H_2 production rate, from which the standard deviation in the measurements was calculated.

Photocatalytic reduction of CO_2. A gas/solid photoreactor setup was assembled to conduct the photocatalytic reduction of CO_2. The as-synthesised, finely ground photocatalysts were deposited on a circular metal disc with a fixed area of 9.6 cm^2. To do so, 30 mg of photocatalyst (B-BNO, Porous BNO, P25 TiO_2, and bulk g-C_3N_4) was added to 1.5 mL of ethanol and stirred rapidly to form a homogeneous suspension, which was drop casted onto the sample holder. The drop casted sample was dried overnight at 120 °C in a drying oven prior to testing. Research grade (99.999%) CO_2 and H_2 (99.9995%, Peak Scientific PH200 hydrogen generator) were flowed at controlled rates using mass flow controllers (Omega Engineering, 0–50 mL/min). Firstly, the photoreactor (35 cm^3) was vacuumed and replenished with a gas mixture of CO_2 and H_2 (1.5 vol/vol ratio) ten times. The same gas mixture of CO_2 and H_2 was subsequently passed over the catalyst bed in the photoreactor for 15 residence times before it was sealed at 1.40 bara and irradiated for 3 hours. A xenon arc lamp (300 W, $\lambda > 325$ nm, LOT Quantum Design), equipped with a water filter was used as the irradiation source with the distance from the lamp to the sample being 9.5 cm and the intensity at the catalyst surface measured to be 1850 ± 17 W m^{-2}. The lamp intensity was measured using a UV-Vis spectrophotometer with 280 – 900 nm range (StellarNet) and an average lamp intensity with standard deviation was calculated after three repeat measurements. The evolved gases were detected by a gas chromatograph (GC, Agilent Technologies) with HayeSep and molecular sieve columns in series, and thermal conductivity (TCD) and flame ionisation (FID) detectors. In addition, isotopic tracing experiments were performed with $^{13}CO_2$ (BOC, >98% atom $^{13}CO_2$ compared to $^{12}CO_2$, >99%). The photocatalytic CO_2 reduction tests were repeated three times for each material under the same reaction conditions to obtain an average specific CO production rate, from which the standard deviation in the measurements was calculated.

Electron paramagnetic resonance (EPR) spectroscopy. EPR experiments were acquired using a Bruker Elexsys E580 CW EPR spectrometer operating at X-band frequencies (9–10 GHz/0.3 T), equipped with a Bruker ER4118-X MD5 resonator. All spectra were recorded at room temperature in air atmosphere in 4mm EPR suprasil tubes. Specifically, the B-BNO data was acquired using a microwave frequency of 9.658 GHz with microwave power 0.2 mW and a 10 Hz modulation with 1G amplitude in the detection sequence. On the other hand, porous BNO measurements required 2 mW power with 100 kHz modulation with 2G amplitude.[35] Simulations were carried out using the EasySpin[52] toolbox running on MATLAB™.

Work function measurements. The work function of B-BNO and porous BNO was determined by measuring the secondary electron cut-off in the low kinetic energy region using a Thermo Scientific K-Alpha$^+$ X-ray Photoelectron Spectrometer equipped with a MXR3 Al Kα monochromated X-ray source (hv = 1486.6 eV). A known mass (100 mg) of sample was pelletized to form a thin, homogeneous pellet, which was clipped to the sample holder. The sample holder contained a clean gold standard sample, which was used as a reference material to ensure correct calibration. A bias of -30 V was applied to the samples using a DC supply and the cut-off spectra were obtained using a pass energy of 10 eV. The connection is made at the bottom of the sample holder and the voltage is activated from the sputter window. The data for the secondary electron cut-off has been processed such that the tangent is taken at the segment of the graph where the data exhibits a linear trend after the initial curve upwards from the x-axis. To do so, we have used linear extrapolation to fit a line of best fit to the linear data range with the corresponding equation and coefficient of determination.

Acknowledgements

The authors would like to acknowledge the funding from EPSRC through the Doctoral Partnership fund (1855454), which made this research possible, and through the EPSRC equipment funding for SPIN-Lab (EP/P030548/1), as well as ERC Starting Grant THEIA (Project Number: 850624).

Declaration

The authors declare that there are no competing financial interests.

References

1. IEA, *World Energy Outlook* **2019**.
2. J.A. Herron, J. Kim, A.A. Upadhye, G.W. Huber, and C.T. Maravelias, *Energy Environ. Sci.* **2015,** *8*, (1), 126.
3. S. Zhang, Y. Zhao, R. Shi, C. Zhou, G.I. Waterhouse, L.Z. Wu, C.H. Tung, and T. Zhang, *Adv. Energy Mater.* **2020,** *10*, (8), 1901973.
4. Z.-K. Shen, Y. Yuan, P. Wang, W. Bai, L. Pei, S. Wu, Z. Yu, and Z. Zou, *ACS Appl. Mater. Interfaces* **2020**.
5. H.-i. Kim, Y. Choi, S. Hu, W. Choi, and J.-H. Kim, *Appl. Catal. B* **2018,** *229*, 121.
6. A. Fujishima and K. Honda, *Nature* **1972,** *238*, (5358), 37.
7. T. Inoue, A. Fujishima, S. Konishi, and K. Honda, *Nature* **1979,** *277*, 637.
8. A. Crake, K.C. Christoforidis, A. Kafizas, S. Zafeiratos, and C. Petit, *Appl. Catal. B* **2017,** *210*, 131.
9. A. Crake, K.C. Christoforidis, R. Godin, B. Moss, A. Kafizas, S. Zafeiratos, J.R. Durrant, and C. Petit, *Appl. Catal. B* **2019,** *242*, 369.
10. A. Crake, K.C. Christoforidis, A. Gregg, B. Moss, A. Kafizas, and C. Petit, *Small* **2019,** *15*, (11), 1805473.
11. T.W. Woolerton, S. Sheard, E. Pierce, S.W. Ragsdale, and F.A. Armstrong, *Energy Environ. Sci.* **2011,** *4*, (7), 2393.
12. T.W. Woolerton, S. Sheard, E. Reisner, E. Pierce, S.W. Ragsdale, and F.A. Armstrong, *J. Am. Chem. Soc* **2010,** *132*, (7), 2132.
13. F. Liao, Z. Zeng, C. Eley, Q. Lu, X. Hong, and S.C.E. Tsang, *Angew. Chem. Int. Ed.* **2012,** *51*, (24), 5832.
14. H. Lin, Y. Liu, J. Deng, S. Xie, X. Zhao, J. Yang, K. Zhang, Z. Han, and H. Dai, *J. Photochem. Photobiol* **2017,** *336*, 105.
15. J. Nunez, A. Víctor, P. Jana, J.M. Coronado, and D.P. Serrano, *Catal. Today* **2013,** *209*, 21.
16. F. Yoshitomi, K. Sekizawa, K. Maeda, and O. Ishitani, *ACS Appl. Mater. Interfaces* **2015,** *7*, (23), 13092.
17. N. Zhang, S. Ouyang, T. Kako, and J. Ye, *ChemComm* **2012,** *48*, (9), 1269.
18. Y.P. Xie, G. Liu, G.Q.M. Lu, and H.-M. Cheng, *Nanoscale* **2012,** *4*, (4), 1267.
19. Y. Cao, R. Zhang, T. Zhou, S. Jin, J. Huang, L. Ye, Z. Huang, F. Wang, and Y. Zhou, *ACS Appl. Mater. Interfaces* **2020,** *12*, (8), 9935.
20. S. Zhou, Y. Liu, J. Li, Y. Wang, G. Jiang, Z. Zhao, D. Wang, A. Duan, J. Liu, and Y. Wei, *Appl. Catal. B* **2014,** *158*, 20.
21. M. Zhou, S. Wang, P. Yang, C. Huang, and X. Wang, *ACS Catalysis* **2018,** *8*, (6), 4928.

22. Z. Sun, J.M.T.A. Fischer, Q. Li, J. Hu, Q. Tang, H. Wang, Z. Wu, M. Hankel, D.J. Searles, and L. Wang, *Appl. Catal. B* **2017,** *216*, 146.
23. J. Lin, Z. Pan, and X. Wang, *ACS Sustain. Chem. Eng.* **2013,** *2*, (3), 353.
24. Y. Zhang and M. Antonietti, *Chem. Asian J.* **2010,** *5*, (6), 1307.
25. L. Acharya, S. Nayak, S.P. Pattnaik, R. Acharya, and K. Parida, *J. Colloid Sci.* **2020,** *566*, 211.
26. M. Campanelli, T. Del Giacco, F. De Angelis, E. Mosconi, M. Taddei, F. Marmottini, R. D'Amato, and F. Costantino, *ACS Appl. Mater. Interfaces* **2019**.
27. S. Yang, W. Hu, X. Zhang, P. He, B. Pattengale, C. Liu, M. Cendejas, I. Hermans, X. Zhang, and J. Zhang, *J. Am. Chem. Soc* **2018,** *140*, (44), 14614.
28. M. Lu, J. Liu, Q. Li, M. Zhang, M. Liu, J.L. Wang, D.Q. Yuan, and Y.Q. Lan, *Angew. Chem.* **2019,** *131*, (36), 12522.
29. W. Zhong, R. Sa, L. Li, Y. He, L. Li, J. Bi, Z. Zhuang, Y. Yu, and Z. Zou, *J. Am. Chem. Soc* **2019,** *141*, (18), 7615.
30. R.S. Sprick, B. Bonillo, R. Clowes, P. Guiglion, N.J. Brownbill, B.J. Slater, F. Blanc, M.A. Zwijnenburg, D.J. Adams, and A.I. Cooper, *Angew. Chem. Int. Ed.* **2016,** *55*, (5), 1792.
31. M. Sachs, R.S. Sprick, D. Pearce, S.A. Hillman, A. Monti, A.A. Guilbert, N.J. Brownbill, S. Dimitrov, X. Shi, and F. Blanc, *Nat. Commun* **2018,** *9*, (1), 1.
32. R.S. Sprick, B. Bonillo, M. Sachs, R. Clowes, J.R. Durrant, D.J. Adams, and A.I. Cooper, *ChemComm* **2016,** *52*, (65), 10008.
33. L. Wang, R. Fernández-Terán, L. Zhang, D.L. Fernandes, L. Tian, H. Chen, and H. Tian, *Angew. Chem. Int. Ed.* **2016,** *55*, (40), 12306.
34. X. Jin, Q. Guan, T. Tian, H. Li, Y. Han, F. Hao, Y. Cui, W. Li, Y. Zhu, and Y. Zhang, *Appl. Surf. Sci.* **2020,** *504*, 144241.
35. R. Shankar, M. Sachs, L. Francàs, D. Lubert-Perquel, G. Kerherve, A. Regoutz, and C. Petit, *J. Mater. Chem. A* **2019,** *7*, (41), 23931.
36. M. Wang, M. Li, L. Xu, L. Wang, Z. Ju, G. Li, and Y. Qian, *Catal. Sci. Technol.* **2011,** *1*, (7), 1159.
37. X. Li, J. Zhao, and J. Yang, *Sci. Rep.* **2013,** *3*, 1858.
38. J. Pang, Y. Chao, H. Chang, H. Li, J. Xiong, M. He, Q. Zhang, H. Li, and W. Zhu, *J. Colloid Sci.* **2017,** *508*, 121.
39. X. Wang, K. Maeda, A. Thomas, K. Takanabe, G. Xin, J.M. Carlsson, K. Domen, and M. Antonietti, *Nat. Mater* **2009,** *8*, (1), 76.
40. C. Huang, C. Chen, M. Zhang, L. Lin, X. Ye, S. Lin, M. Antonietti, and X. Wang, *Nat. Commun* **2015,** *6*, 7698.
41. Q. Weng, Y. Ide, X. Wang, X. Wang, C. Zhang, X. Jiang, Y. Xue, P. Dai, K. Komaguchi, and Y. Bando, *Nano Energy* **2015,** *16*, 19.
42. Z. He, C. Kim, L. Lin, T.H. Jeon, S. Lin, X. Wang, and W. Choi, *Nano Energy* **2017,** *42*, 58.
43. Q. Weng, D.G. Kvashnin, X. Wang, O. Cretu, Y. Yang, M. Zhou, C. Zhang, D.M. Tang, P.B. Sorokin, and Y. Bando, *Adv. Mater.* **2017,** *29*, (28).
44. R. Shankar, S. Marchesini, and C. Petit, *J. Phys. Chem. C* **2019,** *123*, (7), 4282.
45. S. Alkoy, C. Toy, T. Gönül, and A. Tekin, *J. Eur. Ceram. Soc* **1997,** *17*, (12), 1415.
46. C.G. Cofer and J. Economy, *Carbon* **1995,** *33*, (4), 389.
47. M. Florent and T.J. Bandosz, *J. Mater. Chem. A* **2018,** *6*, (8), 3510.
48. L. Rusanova and L. Gorchakova, *J. Sov. Powder Metall. Met. Ceram.* **1980,** *19*, (3), 189.
49. S. Marchesini, A. Regoutz, D. Payne, and C. Petit, *Microporous Mesoporous Mater.* **2017,** *243*, 154.
50. S. Brunauer, P.H. Emmett, and E. Teller, *J. Am. Chem. Soc* **1938,** *60*, (2), 309.
51. S. Chen and R. Yang, *Langmuir* **1994,** *10*, (11), 4244.
52. S. Stoll and A. Schweiger, *J. Magn. Reson.* **2006,** *178*, (1), 42.
53. O.O. Kurakevych and V.L. Solozhenko, *Acta Crystallogr. C* **2007,** *63*, (9), i80.
54. S. Marchesini, C.M. McGilvery, J. Bailey, and C. Petit, *ACS Nano* **2017,** *11*, (10), 10003.
55. R. Geick, C. Perry, and G. Rupprecht, *Phys. Rev.* **1966,** *146*, (2), 543.

56. G. Liu, L.C. Yin, P. Niu, W. Jiao, and H.M. Cheng, *Angew. Chem. Int. Ed.* **2013,** *52*, (24), 6242.
57. Q. Fan, C. Choi, C. Yan, Y. Liu, J. Qiu, S. Hong, Y. Jung, and Z. Sun, *ChemComm* **2019,** *55*, (29), 4246.
58. G. Ciofani, G.G. Genchi, I. Liakos, A. Athanassiou, D. Dinucci, F. Chiellini, and V. Mattoli, *J. Colloid Sci.* **2012,** *374*, (1), 308.
59. V. Cholet, L. Vandenbulcke, J. Rouan, P. Baillif, and R. Erre, *J. Mater. Sci.* **1994,** *29*, (6), 1417.
60. K. Park, D. Lee, K. Kim, and D. Moon, *Appl. Phys. Lett* **1997,** *70*, (3), 315.
61. A.S. Nazarov, V.N. Demin, E.D. Grayfer, A.I. Bulavchenko, A.T. Arymbaeva, H.J. Shin, J.Y. Choi, and V.E. Fedorov, *Chem. Asian J.* **2012,** *7*, (3), 554.
62. K. Watanabe, T. Taniguchi, and H. Kanda, *Nat. Mater* **2004,** *3*, (6), 404.
63. V.I. Matkovich, G.-. Samsonov, and P. Hagenmuller, *Boron and Refractory Borides*. Springer: 1977.
64. A. Panich, A. Shames, N. Froumin, C. Tang, and Y. Bando, *Phys. Rev. B* **2005,** *72*, (8), 085307.
65. K. Simonov, N.A. Vinogradov, M.L. Ng, A. Vinogradov, N. Mårtensson, and A. Preobrajenski, *Surf. Sci.* **2012,** *606*, (3-4), 564.
66. F. Gerson and W. Huber, *Electron Spin Resonance Spectroscopy of Organic Radicals*. John Wiley & Sons: 2003.
67. B.H. Tran, K. Tieu, S. Wan, H. Zhu, S. Cui, and L. Wang, *RSC Adv.* **2018,** *8*, (51), 28847.
68. F. Späth, H.R. Soni, J. Steinhauer, F. Düll, U. Bauer, P. Bachmann, W. Hieringer, A. Görling, H.P. Steinrück, and C. Papp, *Journal of Chemistry - A European Journal* **2019,** *25*, (37), 8884.
69. J. Qu, Q. Li, C. Luo, J. Cheng, and X. Hou, *Journal of Coatings* **2018,** *8*, (6), 214.
70. S. Caneva, M.-B. Martin, L. D'Arsié, A.I. Aria, H. Sezen, M. Amati, L. Gregoratti, H. Sugime, S. Esconjauregui, and J.J.A.a.m. Robertson, *ACS Appl. Mater. Interfaces* **2017,** *9*, (35), 29973.
71. M. Marszewski, S. Cao, J. Yu, and M. Jaroniec, *Mater. Horiz* **2015,** *2*, (3), 261.
72. G. Liao, Y. Gong, L. Zhang, H. Gao, G.-J. Yang, and B. Fang, *Energy Environ. Sci.* **2019,** *12*, (7), 2080.

Table of contents

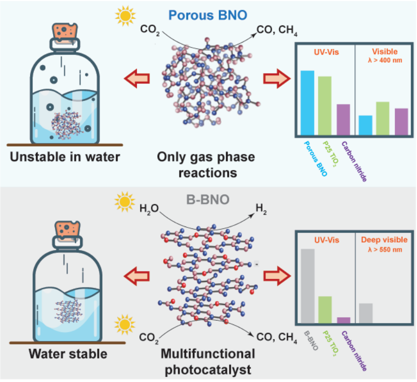

Porous boron oxynitride (BNO), the hitherto benchmark BN-based photocatalyst, is able to capture and convert CO_2 to solar fuels using sunlight. However, the material is restricted by two limitations: (1) it is unstable in water and (2) the performance is low under visible light. Boron-doped boron oxynitride (B-BNO) is presented as a new BN-based photocatalyst that can overcome these bottlenecks.

Keyword: photocatalysis